WILEY-VCH

Efficient Indium-Doped TiO$_x$ Electron Transport Layers for High-Performance Perovskite Solar Cells and Perovskite-Silicon Tandems

Jun Peng,* The Duong, Xianzhong Zhou, Heping Shen, Yiliang Wu, Hemant Kumar Mulmudi, Yimao Wan, Dingyong Zhong, Juntao Li, Takuya Tsuzuki, Klaus J. Weber, Kylie R. Catchpole, and Thomas P. White*

Jun Peng, The Duong, Dr. Heping Shen, Yiliang Wu, Dr. Hemant Kumar Mulmudi, Dr. Yimao Wan, Prof. Takuya Tsuzuki, Prof. Klaus J. Weber, Prof. Kylie R. Catchpole, and Dr. Thomas P. White
 Research School of Engineering, The Australian National University, Canberra, ACT 2601, Australia
E-mail:u5686151@anu.edu.au or pengjun.88.81@gmail.com
E-mail:thomas.white@anu.edu.au

Dr. Xianzhong Zhou, Prof. Dingyong Zhong, Prof. Juntao Li and Dr. Thomas P. White
State Key Laboratory of Optoelectronic Materials & Technologies, School of Physics, Sun Yat-sen University, Guangzhou 510275, China

Abstract

In addition to a good perovskite light absorbing layer, the hole and electron transport layers play a crucial role in achieving high-efficiency perovskite solar cells. Here we introduce a simple, one-step, solution-based method for fabricating high quality indium-doped titanium oxide electron transport layers. We show that indium-doping improves both the conductivity of the transport layer and the band alignment at the ETL/perovskite interface compared to pure TiO$_2$, boosting the fill-factor and voltage of perovskite cells. Using the optimized transport layers, we demonstrate a high steady-state efficiency of 17.9% for CH$_3$NH$_3$PbI$_3$-based cells and 19.3% for Cs$_{0.05}$(MA$_{0.17}$FA$_{0.83}$)$_{0.95}$Pb(I$_{0.83}$Br$_{0.17}$)$_3$-based cells, corresponding to absolute efficiency gains of 4.4% and 1.2% respectively compared to TiO$_2$-based control cells.

In addition, we report a steady-state efficiency of 16.6% for a semi-transparent cell and use it to achieve a four-terminal perovskite-silicon tandem cell with a steady-state efficiency of 24.5%.

1. Introduction

Organometal trihalide perovskite solar cells have recently received tremendous attention as promising candidates for next-generation solar cells due to their low bandgap, high charge mobility, high extinction coefficient and weak exciton binding energy.[1-12] Since 2009, significant research effort has dramatically boosted the power conversion efficiency (PCE) of perovskite solar cells from ~4.0%[1] to 22.1% (certified).[13] In addition to stand-alone cells, the high-efficiency, easy-processing and tuneable bandgap of perovskite cells makes them promising candidates for tandem devices. Perovskite-silicon tandem cells built on conventional crystalline silicon technology are regarded as a highly promising low-cost solution to push efficiencies toward 30%; well above the efficiency limit of single-junction silicon cells.[14-21]

Much of the perovskite cell research to date has focused on improving the crystallinity and the formation of high-quality, uniform perovskite thin films, via one step[2,3] and two-step solution processes,[22] additives[23-26] and anti-solvent treatments,[27,28] thermal evaporation[29] and other methods.[30-36] In addition, many different perovskite compositions have been systematically developed and investigated to improve and enhance the PCE and stability of perovskite solar cells.[4,21,37-41] Other work has focused on reducing the energy barrier of charge injection in perovskite solar cells by developing new kinds of high-performance hole-transporting materials (HTMs)[42,43] and exploiting efficient electron-transporting materials (ETMs) with suitable workfunction (WF) and high conductivity.[9,10,44-59]

To date, most high-efficiency perovskite solar cells have been obtained from devices with a structure of FTO/ETL/Perovskite/HTL/metal contact, where ETL and HTL represent the electron and hole transport layers respectively. The most common HTLs are 2,2',7,7'-Tetrakis-(N,N-di-4-methoxyphenylamino)-9,9'-spirobifluorene (Spiro-OMeTAD) and poly (triaryl amine) (PTAA), which have been proved to be excellent HTMs with high charge mobility and efficient electron-blocking property.[4,5,9,41] Titanium oxide (TiO_2) is the most common ETL, and has been widely used in perovskite solar cells due to its good chemical resistance, electronic and optical properties, as well as being compatible with a variety of deposition methods.[2,5,22] Pure TiO_2-based perovskite solar cells typically produce high short-circuit current density (J_{sc}), but can suffer from lower open circuit voltage (V_{oc}) and fill factor (FF), which limits their PCE. Thus, highly conductive TiO_x[46,59] and its dopants,[9,45,60-62] ZnO[44] and its dopants,[47,63] SnO_2[55,56] and n-type organic materials[51,53,58,64] have all been investigated as alternative ETLs. For example, Zhou *et al* [9] reported Y-doped TiO_2 used as an efficient ETL for perovskite solar cells, yielding a high PCE of 19.3% with a V_{oc} of 1.13 V and FF of 0.75. In 2016, Giordano *et al*[45] reported a PCE of more than 19% with negligible hysteretic behaviour using Li-doped meso-TiO_2 as a scaffold for the perovskite active layer. Al-doped TiO_2[61] and Zn-doped TiO_2[62] have also been reported, although the PCEs were relatively low. In addition, more complex bilayer-structure ETLs consisting of metal oxides and organic materials, such as TiO_x/PCBM,[54] TiO_2/Graphene,[48] SnO_2/C_{60},[49] PEIE/Y-TiO_2[9] and the like[50,52] have also been developed. Many of these ETL variations have been shown to increase either the FF or V_{oc} of perovskite solar cells through improved conductivity[44,48,59] or improved band alignment[52] respectively, but only a small number have successfully increased both cell parameters simultaneously.[9,45,54] Hence, there remains a large space for improving both the FF and V_{oc} in perovskite solar cells by optimizing ETLs to have a suitable WF and good conductivity.

In this work, we demonstrate a solution-processed In-TiO$_x$ as an efficient ETL for perovskite solar cells, where the precursor of In-TiO$_x$ can be easily obtained by mixing the indium precursor with the TiO$_2$ precursor in the correct proportions. The conductivity of compact In-TiO$_x$ thin films increases due to the indium dopant, thus dramatically improving the FF of perovskite solar cells compared to cells with pure TiO$_2$ ETLs. Furthermore, indium-doping allows us to tune the work function of the ETL to improve the band alignment at the ETL/perovskite interface. Consequently, we obtained high efficiencies of 18.9% for CH$_3$NH$_3$PbI$_3$-based (MAPbI$_3$) solar cells and 20.1% for Cs$_{0.05}$(MA$_{0.17}$FA$_{0.83}$)$_{0.95}$-Pb(I$_{0.83}$Br$_{0.17}$)$_3$-based cells. These cells exhibit impressive FF values of 0.771 and 0.791, respectively, which are among the highest values reported for TiO$_x$-based perovskite solar cells.[4,9,12,39,41,54] We also apply the optimized ETL to semi-transparent perovskite cells, achieving a steady-state efficiency of 16.6%, and use these cells to demonstrate a four-terminal perovskite-silicon tandem cell with an efficiency of 24.5%.

2. Results and Discussion

In the following sections, we systematically characterize the physical, electrical and optical properties of In-TiO$_x$ thin films on various substrates using x-ray photoelectron spectroscopy/ultraviolet photoelectron spectroscopy (XPS/UPS), atomic force microscopy (AFM), optical transmittance, impedance spectroscopy and Hall Effect measurements. We directly compare these properties to un-doped compact TiO$_2$ ETLs as typically used in perovskite cells. These results are further supported by electron microscope (SEM), x-ray diffraction (XRD) and device characterization to further investigate the performance of In-TiO$_x$ and TiO$_2$-based perovskite solar cells. Detailed information for In-TiO$_x$ processing and device fabrication can be found in experimental section.

2.1. XPS and UPS analysis

4

In-TiO$_x$ thin films for XPS/UPS and AFM characterizations were prepared according to our best indium-doping condition (3%-In-TiO$_x$). XPS measurements were conducted to elucidate the chemical compositions of TiO$_2$ and In-TiO$_x$ deposited on FTO substrates. **Figures 1**a,b compare the XPS spectra of the Ti 2p and In 3d peaks respectively for the two films. Figure 1a shows the Ti 2p1 and Ti 2p3 peaks of the TiO$_2$ film at binding energies of ~464.3 eV and ~458.5 eV, which are consistent with literature values.[65] For the In-TiOx films, the Ti 2p3 peak is shifted slightly higher to 458.8 eV. This shift can be explained by the Pauling electronegativity theory; the electronegativity value of Ti is 1.5 and In is 1.7, which indicates negative charge transfer towards indium in the Ti-O-In bond, thereby increasing the Ti 2p core level binding energy.[65] Figure 1b shows the XPS spectrum of In 3d5 for the In-TiO$_x$ film, with a single peak centred at ~444.3 eV that can be ascribed to indium oxide.[65] As expected, the TiO$_2$ does not have a corresponding peak. The surface stoichiometry of the samples was calculated by comparing the elements' relative peak areas and their corresponding relative sensitivity factors. The atomic ratio of Ti:O for TiO$_2$ sample is about 1:2, and the atomic ratio of In:Ti for In-TiO$_x$ is 2:98. Detailed analysis of O 1s peaks for In-TiO$_x$ and TiO$_2$ is also provided in Figure S1a (Supporting Information). Samples prepared on ITO substrates were found to have very similar XPS spectra as shown in Figure S1b-d (Supporting Information).

UPS measurements were also performed to estimate the WF of FTO/TiO$_2$ and FTO/In-TiO$_x$ samples. Figure 1c shows that the photoemission cutoff of bare FTO is 16.65 eV corresponding to a WF of ~4.55 eV, while the WF of FTO/TiO$_2$ is ~4.22 eV. To better investigate the WF of the FTO/In-TiO$_x$, we prepared films with four different indium doping concentrations varying from 1% to 7% (v/v), labelled as 1%-In-TiO$_x$ to 7%-In-TiO$_x$. As depicted in Figure 1c, the WF initially decreases with increasing indium concentration from ~4.06 eV for 1%-In-TiO$_x$ to ~4.00 eV for 3%-In-TiO$_x$. With additional indium content, the WF increases again, to ~4.02 eV for 5%-In-TiO$_x$ and ~4.06 eV for 7%-In-TiO$_x$, which is the

5

same as for 1%-In-TiO$_x$. For all doping levels, the WF of In-TiO$_x$ is closer to the conduction band (CB) of MAPbI$_3$ perovskite (~3.9 eV)[66] than that of TiO$_2$ shown in **Figure 2**a. We show later that this translates into higher V_{oc} values for MAPbI$_3$-based solar cells with In-TiO$_x$ ETLs compared to those with TiO$_2$ ETLs. UPS spectra were also obtained for ITO/TiO$_2$ and ITO/In-TiO$_x$ samples (see Figure S2a, Supporting Information). The WF of ITO/TiO$_2$ and ITO/In-TiO$_x$ are similar to those of FTO/TiO$_2$ and FTO/In-TiO$_x$, further proving the band alignment of In-TiO$_x$ is better than that of pure TiO$_2$ for MAPbI$_3$-based device structures.

The role of In as a dopant in TiO$_x$ may be ascribed to the following explanations. From the Ti 2p XPS data of In-TiO$_x$ and TiO$_2$ in Figure 1a, we observe a Ti 2p core-level shift with indium doping. This shift is caused by a charge transfer effect in the Ti-O-In bond, indicating that the indium ions are incorporated into the TiO$_2$ lattice.[61,65] According to Pathak *et al*,[61] Giordano *et al*[45] and Rourke *et al*[67], oxygen vacancies, Ti interstitial sites and non-stoichiometric oxygen-induced defects or trap states within the TiO$_2$ lattice can trap injected electrons, and act as recombination centres. These works reported that a small amount of extrinsic dopants with valency +3 (such as Al^{3+} ions) can effectively passivate/remove the defect or trap states, reduce the sub-bandgap states and raise the conduction band.[45,61,67] According to our UPS results (Figure 1c) and Hall Effect measurements (Table S1, Supporting Information), the WF of In-TiO$_x$ is lower than that of pure TiO$_2$, and the carrier density for In-TiOx is higher than that of pure TiO$_2$, suggesting that In-doping reduces the density of sub-bandgap states and increases the electron conductivity. Therefore, the In^{3+} doping mechanism might be consistent with that of the Al-doped TiO$_2$.[61] Thus, a low level of In-doping can passivate the electronic defects or trap states caused by non-stoichiometric oxygen-induced defects within the TiO2 lattice,[45,61] resulting in improved electron transport properties and band alignment for perovskite solar cells.

2.2. AFM & Transmittance Analysis

AFM was used to probe the surface morphology of the solution-processed ~50 nm TiO_2 and In-TiO_x films deposited on both FTO and ITO substrates (see Figure S3, Supporting Information). Measurements of FTO/In-TiO_x (FTO/TiO_2) samples show a continuous and conformal film with rms roughness of ~17.2 nm (~17.5 nm), compared to ~28.3 nm for the bare FTO. ITO/TiO_2 and ITO/In-TiO_x samples have roughness of 1.31 nm and 1.29 nm respectively, compared to 3.8 nm for bare ITO. These results confirm that the In-TiO_x film provides a dense and compact transport layer on multiple substrate types.

In addition to high quality conformal films, it is also essential for the In-TiO_x to have a high transmittance to maximize the current of perovskite solar cells. Figure 2b demonstrates that the transmittance of FTO/In-TiO_x samples is almost identical to that of FTO/TiO_2. Note that all of the coated samples have lower transmittance than the bare FTO due to increased reflectance resulting from the high refractive index TiO_2/In-TiO_x films. Transmittance spectra for ITO-based samples are provided in Figure S2b (Supporting Information) and show similar behaviour. We therefore conclude that the indium doping has a negligible effect on the optical properties of the TiO_2/In-TiO_x films.

2.3. MAPbI$_3$ cell performance with In-TiO_x ETL

We used a normal device structure, consisting of FTO/In-TiO_x(or TiO_2)/meso-TiO_2/MAPbI$_3$/Spiro-OMeTAD/Au (see Figure 2c), to verify the performance improvement provided by the In-TiO_x ETL compared to cells with a pure TiO_2 ETL. Figure 2d shows a SEM cross-sectional image of a complete cell. The thickness of the In-TiO_x film and mesoporous TiO_2 layers are ~55 nm and ~75 nm respectively, capped by ~280nm of MAPbI$_3$ and 180nm of Spiro-OMeTAD.

To optimize the performance of In-TiO_x-based cells, we prepared cells on FTO substrates using indium doping concentrations varying from 0% to 7% (v/v), labelled as TiO_2, 1%-In-

TiO$_x$, 3%-In-TiO$_x$, 5%-In-TiO$_x$ and 7%-In-TiO$_x$. **Figure 3** shows the measured values of V_{oc}, J_{sc}, FF and PCE of 100 different cells as a function of indium concentration. Figure 3a shows that even 1% indium doping can dramatically improve the V_{oc} from ~1.04 V (the median V_{oc} for TiO$_2$) to ~1.07 V (median V_{oc} for 1%-In-TiO$_x$). The V_{oc} reached a maximum median value of 1.09 V for the 3%-In-TiO$_x$. A slightly decreased V_{oc} (~1.085 V) was observed with the 5% indium doping concentration before the V_{oc} drops back to ~1.07 V for the 7%-In-TiO$_x$. This trend is consistent with the UPS measurements of the WF of In-TiO$_x$ and TiO$_2$ discussed in the UPS section.

The statistical distribution of FF for the TiO$_2$ and In-TiO$_x$-based cells shows a similar trend to that of V_{oc} (see Figure 3b). A median FF of 0.665 was obtained from TiO$_2$-based control cells, whereas the 3%-In-TiO$_x$-based cells exhibited a median FF of ~0.750, corresponding to a ~13% improvement. Comparing to the current density vs voltage (J-V) curve of In-TiO$_x$-based and TiO$_2$-based cells shown in **Figure 4**a, it appears that the improved FF is largely due to a reduced series resistance in the In-TiOx-based cells. Therefore, Hall Effect measurements were employed to further study the electronic properties of the ETL layer. The results in Table S1 (Supporting Information) show that the conductivity of In-TiO$_x$ is higher than that of TiO$_2$, which is possibly caused by the increased carrier density and hall mobility, thus reducing the series resistance in In-TiO$_x$-based cells.[9,59] We also note that the conductivity of In-TiO$_x$ shows a similar trend to the WF of In-TiO$_x$; initially increasing with indium content up to concentrations of 3%~5%, then decreasing again for higher doping levels.

In Figure 3c, the median J_{sc} for In-TiO$_x$-based cells shows only a weak variation with indium content, where the median J_{sc} of 22.09 mA/cm^2 for 3%-In-TiO$_x$-based cells is slightly (~4%) higher than that of the TiO$_2$-based control devices (J_{sc} ~21.3 mA/cm^2). Indeed, the data of XRD and SEM (Figure S4, Supporting Information) shows that MAPbI$_3$ thin films deposited on Glass, FTO/TiO$_2$ and FTO/In-TiO$_x$ substrates exhibited similar coverage and crystallinity, so we would not expect significant variation in J_{sc}. The combination of higher V_{oc} and FF, and

J_{sc} results in an absolute efficiency increase of more than ~3.3% for 3%-In-TiO$_x$-based cells (PCE$_{median}$~17.8%) as compared to the TiO$_2$-based control cells (PCE$_{median}$~14.5%) (see Figure 3d).

Furthermore, we used impedance spectroscopy to investigate the series resistance, interfacial and bulk recombination within the In-TiO$_x$-based and TiO$_2$-based perovskite cells. As shown in Figure S5, the series resistance extracted from the In-TiO$_x$-based perovskite cell is significantly lower than that of TiO$_2$-based perovskite cell. In addition, the bulk charge recombination lifetimes for both cells show no significant difference. However, the surface charge recombination lifetime for the In-TiO$_x$-based perovskite cell is higher than that of of the TiO$_2$-based perovskite cell. This further supports the conclusion that the improved cell performance results from higher conductivity and improved interface properties of the In-TiO$_x$-based ETL.

J-V curves of MAPbI$_3$-based cells with In-TiO$_x$ and TiO$_2$ ETLs are shown in Figure 4a. Our champion In-TiO$_x$-based cell had a PCE of 18.9% with J_{sc}=22.3mA/cm^2, V_{oc}=1.10 V and FF=0.771, measured by reverse J-V scan. The best TiO$_2$-based control device, exhibited a PCE of 16.3%, with V_{oc}=1.06 V, J_{sc}=22.1 mA/cm^2 and FF=0.706. Forward scanning and steady-state efficiency measurements were also performed to verify the cell performance. As shown in Figure 4b, the steady-state efficiency of the In-TiO$_x$-based cell is 17.9% after holding it at a constant bias voltage of 0.91 V for 170 s. The corresponding efficiency of the TiO$_2$-based control device was 13.5% at a bias of 0.81 V, also after 170 s of continuous measurement (see Figure S6a, Supporting Information). Since the cells exhibit some hysteresis between forward and reverse scans, the bias voltage for these steady-state measurements was chosen as the average of the maximum power point voltage (V_{mpp}) of the two scan directions. With In-TiO$_x$-based cells, as shown in Fig. 4a, we observed a small reduction in hysteresis compared with the TiO$_2$-based control devices. This may be attributed to the In-doping passivating the electronic defects or trap states caused by non-stoichiometric

9

oxygen-induced defects within the TiO_2 lattice,[45,61] thus supressing the perovskite cell's hysteresis.[45]

Figure 4c shows the reverse (forward) scanning *J-V* curves of the best $ITO/In\text{-}TiO_x$-based cell with an efficiency of 18.8% (17.4%) and the ITO/TiO_2-based control cell with an efficiency of 16.1% (14.5%). This further confirms that the performance of $In\text{-}TiO_x$-based cells is significantly higher than that of control cells with a pure TiO_2 ETL. The corresponding steady-state efficiencies are shown in Figure 4d and Figure S6b (Supporting Information). We also observed a slightly (~3%) increased J_{sc} for ITO-based cells as compared to FTO-based cells due to the higher transmittance of the ITO substrates, as seen in Figure 2b and Figure S2b (Supporting Information). All photovoltaic parameters of the devices are summarized in **Table 1**. In addition, long time steady-state efficiencies for another batch of $FTO/In\text{-}TiO_x$ and $ITO/In\text{-}TiO_x$ $MAPbI_3$-based cells are also provided in Figure S7 (Supporting Information).

2.4. Cs-mixed halide-based perovskite cells

Recently, Saliba *et al*[39] reported high efficiency and stable perovskite cells based on a cesium-containing triple cation perovskite absorber material: $Cs_{0.05}(MA_{0.17}FA_{0.83})_{0.95}Pb(I_{0.83}Br_{0.17})_3$. We also applied the optimized $In\text{-}TiO_x$ ETLs in $Cs_{0.05}(MA_{0.17}FA_{0.83})_{0.95}Pb(I_{0.83}Br_{0.17})_3$-based perovskite cells to study the compatibility of $In\text{-}TiO_x$ with different perovskite compositions. By combining the 3%-$In\text{-}TiO_x$ ETL (the best indium doping condition) with a $Cs_{0.05}(MA_{0.17}FA_{0.83})_{0.95}Pb(I_{0.83}Br_{0.17})_3$ perovskite active layer, we obtained a high PCE of 20.1% from the reverse scan and a corresponding PCE of 18.7% from the forward scan, whereas the TiO_2-based control cell exhibited a PCE of 18.8% and 17.6% respectively (see **Figure 5**a). Detailed results of the best devices are presented in Figure 5a and summarized in **Table 2**. $ITO/In\text{-}TiO_x$ and ITO/TiO_2-based $Cs_{0.05}(MA_{0.17}FA_{0.83})_{0.95}Pb(I_{0.83}Br_{0.17})_3$ perovskite cells were also investigated (see Figure 5c and Table 2). Figures 5b,d show a steady-state efficiency of 19.3% after   200 s operation at a

bias voltage of 0.92 V for the FTO/In-TiO$_x$-based cell, and 18.4% for the ITO/In-TiO$_x$-based

cell. The control FTO/TiO$_2$ and ITO/TiO$_2$-based cells had PCEs of 18.1% (tested at 0.88 V)

and 17.4% (tested at 0.87 V) as shown in Figure S8 (Supporting Information). Device

performance distributions of the FTO/In-TiO$_x$-based and ITO/In-TiO$_x$-based cells are

provided in Figure S9 (Supporting Information), demonstrating that the high performance In-

TiO$_x$-based cells are repeatable.

2.5. Four-terminal Tandem Cells

Encouraged by the high performance of In-TiO$_x$-based perovskite cells, we have also applied

the doped In-TiOx transport layer in a semi-transparent perovskite cell for use as a top cell in

a four-terminal perovskite-silicon tandem cell. In a previous work, we reported a perovskite-

silicon tandem with an efficiency of 20.1% by combining a 12.4% efficient semi-transparent

CH$_3$NH$_3$PbI$_3$ cell with a 19.6% crystalline Si PERL cell.[68] Here we take advantage of the

excellent performance of the Cs-mixed halide perovskite/In-TiOx ETL cells from the previous

section, combined with a high-efficiency interdigitated back contact (IBC) silicon cell to

demonstrate a steady-state tandem efficiency of 24.5%.

While cells on FTO substrates achieved the highest efficiencies, as reported above, we choose

ITO substrates for the semi-transparent cells due to their higher optical transmittance in the

near infrared region. A SEM cross-sectional image of the semi-transparent perovskite cell is

shown in **Figure 6**a with the structure Glass/ITO/In-TiO$_x$/meso-TiO$_2$/Perovskite/Spiro-

OMeTAD/MoO$_3$/ITO/Au, where the perovskite composition is

Cs$_{0.05}$(MA$_{0.17}$FA$_{0.83}$)$_{0.95}$Pb(I$_{0.83}$Br$_{0.17}$)$_3$, and the Au is a gold-finger contact. The measured

thickness of each layer is shown in the same figure. A photo of the completed cell is also

shown as an inset to Figure 6c. Figure 6b and **Table 3** show the performance characteristics of

the best semi-transparent perovskite cell (see Supporting Information Figure S10a, for the

performance distribution of multiple cells). We measure a reverse scan PCE of 17.4 % for the

semi-transparent cell, with V_{oc} = 1.1 V, J_{sc} = 21.5 mA/cm^2 and FF = 0.735. The corresponding forward scan PCE is 15.3 %.

Compared with the opaque cell, the main losses for the semi-transparent cells are in the J_{sc} and FF. The reduction of the J_{sc} is dominated by reduced absorption in the perovskite cell as a result of removing the reflective rear electrode, and is similar to that reported in our previous work on semi-transparent CH$_3$NH$_3$PbI$_3$ cells.[68] The lower FF is attributed to increased resistance of the HTM layers and increased recombination at the HTM interfaces caused by the insertion of ~13 nm MoO$_3$ and the ~40 nm sputtered ITO/gold finger contact design. Figure 6c shows a steady-state PCE of 16.6% for the semi-transparent cell after 200 s at 0.82 V, and a PCE of ~16.4% after 2000 s of continuous testing. Figure 6b also shows the J-V curve of the ~24.0% IBC silicon cell under full illumination, which reduces to a PCE of 7.9% under illumination of light filtered through a semi-transparent perovskite cell (see Table 3). Thus, we have demonstrated a combined steady state efficiency of ~24.5% for a four-terminal tandem cell consisting of a mechanically-stacked semi-transparent perovskite cell (top cell) on an IBC silicon cell (bottom cell). Figure 6d shows the measured EQE of the silicon cell with and without the perovskite cell filter. The measured transmittance of the filter and the predicted EQE (calculated as the product of the filter's transmittance and the measured silicon cell EQE without a filter) of the silicon cell are also plotted, showing excellent agreement. The integrated current densities of the silicon cell with and without the filter are in close agreement with the J-V data shown in Table 3. Measured EQE and absorption spectra of a semi-transparent cell are shown in Figure S11b (Supporting Information). In addition, the EQE of an equivalent ITO/In-TiO$_x$/Cs-mixed halide-based opaque cell is also provided in Figure S11a (Supporting Information). The integrated J_{sc} for the semi-transparent cell and opaque cell from the EQE measurements are within 10% of the corresponding J_{sc} values obtained from J-V scans.

We have also tested the stability of the semi-transparent cells over longer time periods. As shown in Figure S10b (Supporting Information), a cell with an initial PCE of 16.3% only dropped to 15.5% after ~19000 s of continuous operation at a bias voltage of 0.82 V. This confirms the In-TiO$_x$-based semi-transparent cell can retain a reasonable PCE under constant light illumination of several hours.[69] Note that all cells in this work were unencapsulated.

3. Conclusion

In summary, we have demonstrated a solution-processed In-TiO$_x$ as an efficient ETL for perovskite solar cells, where the precursor of In-TiO$_x$ can be easily prepared by mixing the indium precursor with the TiO$_2$ precursor in the correct proportions. The indium-doping improves the efficiency of perovskite cells through two separate mechanisms. First, it increases the carrier density and hall mobility, and hence the conductivity of the In-TiO$_x$ ETL compared to the standard TiO$_2$ ETL, dramatically improving the FF of a range of cells with different substrate materials and perovskite compositions. Second, the indium-doping allows us to tune the work function of the ETL to improve the band alignment at the ETL/perovskite interface. Using this optimized ETL we obtained a high steady-state efficiency of 17.9% for MAPbI$_3$-based cells and 19.3% for Cs$_{0.05}$(MA$_{0.17}$FA$_{0.83}$)$_{0.95}$Pb(I$_{0.83}$Br$_{0.17}$)$_3$ cells, corresponding to absolute efficiency gains of 4.4% and 1.2% respectively compared to control cells with pure TiO$_2$ ETLs. In addition, we demonstrated a high steady-state PCE of 16.6% for a semi-transparent cell and used it to achieve a steady-state efficiency of 24.5% for four-terminal perovskite-silicon tandem cell. This is one of the highest efficiencies reported to date for perovskite-silicon tandem cells.[14-21]

4. Experimental Section

Precursor solutions

13

TiO₂ precursor solution. The TiO_2 precursor solution was prepared according to the Ref.[46], which contains 369 µl titanium isopropoxide (TTIP) (Sigma Aldrich, 99.999%) and 35 µl 2M HCl in 5 mL anhydrous isopropanol.

In-TiOₓ precursor solution. First, 90 mg indium acetate (Sigma Aldrich, 99.99%) was degassed in a round-bottom flask for 6 hours before adding 6 mL anhydrous Pyridine (Sigma Aldrich). The solution was then held at 40 ℃ and stirred for 48 hours to form a transparent solution, then filtered with a 0.45 µm pore-sized PTFE filter. Second, the as-prepared indium source precursor solution was added to the TiO_2 precursor solution to achieve the desired indium doping concentration (v/v). Finally, the indium-containing TiO_2 precursor solution was stirring at room-temperature for 6 hours to form a clear and transparent solution before use. The best 3%-In-TiO_x precursor solution contains 3% (v/v) indium source precursor solution and 97% (v/v) TiO_2 precursor solution.

Perovskite precursor solution. MAPbI3 precursor solution was prepared by dissolving 1 mol MAI and I mol PbI_2 in 1mL anhydrous DMSO:DMF (8:2, v/v). The $Cs_{0.05}(MA_{0.17}FA_{0.83})_{0.95}Pb(I_{0.83}Br_{0.17})_3$ precursor solution was prepared according to the Ref.[39], which contains CsI (0.065M), FAI (1.1 M), PbI_2 (1.2M), MABr (0.2 M) and $PbBr_2$ (0.2 M) in anhydrous DMF:DMSO (4:1, v/v).

Spiro-OMeTAD solution. Spiro-OMeTAD solution was prepared by dissolving 72.5 mg Spiro-OmeTAD, 28.5 µl 4-tert-butypyridine and 17.5 µl of lithium bis(trifluoromethanesulfonyl)imide solution (520 mg/ml in acetonitrile) in 1 mL Chlorobenzene. Note that after spin-coating the Spiro-OMeTAD solution, the substrates are placed in a humidity-control box for 12 hours to ensure sufficient oxidation of the Spiro-OMeTAD film prior to electrode/contact layer deposition.

Device fabrication and J-V measurement

~50 nm In-TiO$_x$ (or TiO$_2$) compact layers were deposited on the pre-cleaned FTO (~7 Ω/□, Deysol) and ITO (~8-12 Ω/□, Sigma Aldrich) substrates via spin coating the In-TiO$_x$ (or TiO$_2$) precursor solution at 2000 rpm for 30 s. These were then sintered at 500 °C for 30 min, and left to cool down to room temperature. Next, ~80 nm meso-TiO$_2$ was deposited on the In-TiO$_x$ (or TiO$_2$) compact layer via spin coating the meso-TiO$_2$ paste solution for 30 s at 5000 rpm with a ramp of 5000rpm s^{-1}, where the meso-TiO$_2$ paste solution was prepared from 30 nm TiO$_2$ particle paste (30 NR-D, Dyesol) diluted in anhydrous Ethanol (1:9, w/w). After the spin coating, the samples were annealed at 100 °C for 10 min, then sintered at 500 °C for 30 min under air, and allowed to cool down to room temperature.

For MAPbI$_3$-based perovskite cell. MAPbI$_3$ thin film was deposited by spin coating the MAPbI$_3$ precursor solution at 3500 rpm with a ramp of 3500 rpm s^{-1} for 50 s. During this process, around 200 µl Chlorobenzene was poured on the spinning substrates after 10 s. Substrates were then annealed at 100 °C for 10 min. Then, Spiro-OMeTAD thin film was deposited via spin coating at 3000 rpm with a ramp of 3000 rpm s^{-1} for 40 s. Finally, ~100 nm gold was deposited through by a mask (cell's effective area, 0.16 cm^2). Note that all depositions were conducted in a nitrogen-filled glovebox.

For Cs$_{0.05}$(MA$_{0.17}$FA$_{0.83}$)$_{0.95}$Pb(I$_{0.83}$Br$_{0.17}$)$_3$-based perovskite cell. Cs$_{0.05}$(MA$_{0.17}$FA$_{0.83}$)$_{0.95}$-Pb(I$_{0.83}$Br$_{0.17}$)$_3$ thin film was deposited by a two-step spin coating program: first at 2000 rpm with a ramp of 200 rpm s^{-1} for 10 s, and then at 6000 rpm with a ramp of 2000 rpm s^{-1} for 20 s. During the second step, around 100 µl Chlorobenzene was poured on the spinning substrates 5 s prior to the end of the program. Substrates were then annealed at 100 °C for 10 min. Then, Spiro-OMeTAD thin film was deposited via spin coating at 3000 rpm with a ramp of 3000 rpm s^{-1} for 40 s. Finally, ~100 nm gold was deposited through by a mask (cell's effective area, 0.16 cm^2). Note that all depositions were conducted in a nitrogen-filled glovebox.

For four-terminal tandem cell. The semi-transparent perovskite cell (top cell) was fabricated in the following steps. (1) ~50 nm In-TiO$_x$ and ~80 nm meso-TiO$_2$ were sequentially

deposited on ITO substrate as described above. (2) ~450 nm $Cs_{0.05}(MA_{0.17}FA_{0.83})_{0.95}Pb(I_{0.83}Br_{0.17})_3$ capping layer was deposited onto ITO/In-TiO$_x$/meso-TiO$_2$ substrate as decribed above. (3) ~180 nm Spiro-OMeTAD thin film was coated on the top of perovskite thin film. (4) ~13 nm MoO$_x$ was thermally-evaporated on the Spiro-OMeTAD and ~40 nm ITO was deposited on MoO$_x$ layer via sputtering. (5) ~180 nm thick gold-finger contacts were deposited on the sputtered ITO through a shadow mask (cell's effective area, 0.36 cm^2), where the length and width of gold-finger is 6 mm and 50 µm respectively with a surface coverage of ~3%. (6) ~110 nm MgF$_2$ anti-reflection layer was deposited on the glass side and 180 nm MgF$_2$ was deposited on the rear side of the semi-transparent cell. A 2.5 cm×2.5 cm semi-transparent cell used as the filter was also fabricated according to the aforementioned steps; all parameters for the filter are identical to those of the semi-transparent cell. The interdigitated back contact (IBC) silicon cell (bottom cell) was fabricated according to Ref.[70].

J-V measurement. All devices were tested under 1 sun conditions (100 mW/cm^2, AM 1.5G, 25 ^{o}C) in a solar simulator system (model #SS150 from Photo Emission Tech Inc) equipped with a Xenon lamp. The light intensity was calibrated using a certified Fraunhofer CalLab reference cell. For the perovskite solar cells, all cells' *J-V* curves were tested at a 50 mV/s scan rate in a custom-built vacuum measurement jig without aperture mask. Since the cells exhibit some hysteresis between forward and reverse scans, the bias voltage for the steady-state measurements was chosen as the average of the maximum power point voltage (V_{mpp}) of the reverse and forward scan directions. Note that reverse scan is from V_{oc} to J_{sc} (forward bias → short circuit, 1.2 V → -0.1V), and forward scan is from J_{sc} to V_{oc} (short circuit → forward bias, -0.1 V → 1.2 V). No preconditioning protocol has been used before the characterization. The light *J-V* behaviours of IBC silicon cell with/without the filter were measured under standard one sun conditions (100 mW/cm^2, AM 1.5G, 25 ^{o}C) with a 2 cm×2 cm aperture mask.

16

The external quantum efficiency (EQE) spectra of IBC silicon cell with/without the filter were tested under air using a Protoflex Corporation QE measurement AC-Mode system (QE-1400-03).

The external quantum efficiency (EQE) spectra of opaque and semi-transparent cells were measured with a modified Protoflex QE1400 system without light bias in DC mode using a tungsten light source, two Keithey 2425 sourcemeters, and a reference cell. The EQE response was calibrated using a certified Fraunhofer CalLab reference cell.

All cells in this work were unencapsulated.

Characterization

XPS and UPS. X-ray photoelectron spectroscopy (XPS) and ultraviolet photoelectron spectroscopy (UPS) measurements were carried out on an XPS machine (Escalab 250 Xi, Thermo Fisher), with a monochromatic Al K_α (1486.7 eV) X-ray source for XPS and a He I (21.2 eV) gas discharge lamp for UPS. Note that the XPS samples (FTO/In-TiO$_x$ and ITO/In-TiO$_x$) were prepared via spin coating the 3%-In-TiO$_x$ precursor solution.

AFM and SEM. A tapping mode atomic force microscope (Multimode, Bruker) and a FEI Verios scanning electron microscope (SEM) were used to investigate the surface morphology of samples. A Helios Nanolab 600 FIB system was used to prepare cross-sectional SEM images of the cells. Note that the FTO/In-TiO$_x$ and ITO/In-TiO$_x$ samples were deposited by spin coating the 3%-In-TiO$_x$ precursor solution.

Transmittance. A PerkinElmer Lambda 1050 UV/Vis/NIR spectrophotometer was used to investigate the transmittance of samples.

XRD. X-ray diffraction analysis was performed with a Bruker D2 Phaser diffractometer operated at 30 kV, 10 mA at 2θ (Cu Kα) 10–80°, step 0.02° and scan speed 2.3° min^{-1}.

Hall Effect measurement. Hall Effect and resistivity measurements were performed with the four contacts van der Pauw method using Lake Shore 7704A. Note that the structure of

sample for Hall Effect measurement is Glass/In-TiOx (or TiO2)/Au, where the thickness of In-TiOx (or TiO2) and gold contact are about 50 nm and 200 nm respectively. Current (10 nA) reversal were used to remove the unwanted effects of thermal electric. The magnetic field was kept between 0.1 - 0.4 T, positive to negative, through the measurement to remove the influence misalignment voltage. All samples were measured in air, under a dark environment, and at room temperature.

Impedance Spectroscopy: A Auto-Lab (MEP) workstation was used as a frequency response analyser, and impedance measurements were performed in the 1.7 MHz to 1 Hz frequency range. Impedance data were analyzed using Zview equivalent circuit modelling software.

Supporting Information
Supporting Information is available from the Wiley Online Library or from the author.

Received: ((will be filled in by the editorial staff))
Revised: ((will be filled in by the editorial staff))
Published online: ((will be filled in by the editorial staff))

[1] A. Kojima, K. Teshima, Y. Shirai, T. Miyasaka, *J. Am. Chem. Soc.* **2009**, *131*, 6050.
[2] M. M. Lee, J. Teuscher, T. Miyasaka, T. N. Murakami, H. J. Snaith, *Science* **2012**, *338*, 643.
[3] H. S. Kim, C. R. Lee, J. H. Im, K. B. Lee, T. Moehl, A. Marchioro, S. J. Moon, R. Humphry-Baker, J. H. Yum, J. E. Moser, M. Gratzel, N. G. Park, *Sci. Rep.* **2012**, *2*, 591.
[4] W. S. Yang, J. H. Noh, N. J. Jeon, Y. C. Kim, S. Ryu, J. Seo, S. I. Seok, *Science* **2015**, *348*, 1234.

[5] X. Li, D. Bi, C. Yi, J. D. Décoppet, J. Luo, S. M. Zakeeruddin, A. Hagfeldt, M. Grätzel, *Science* **2016**. Available online. doi:10.1126/science.aaf8060.

[6] S. D. Stranks, G. E. Eperon, G. Grancini, C. Menelaou, M. J. Alcocer, T. Leijtens, L. M. Herz, A. Petrozza, H. J. Snaith, *Science* **2013**, *342*, 341.

[7] G. Xing, N. Mathews, S. Sun, S. S. Lim, Y. M. Lam, M. Gratzel, S. Mhaisalkar, T. C. Sum, *Science* **2013**, *342*, 344.

[8] W. Nie, H. Tsai, R. Asadpour, J. C. Blancon, A. J. Neukirch, G. Gupta, J. J. Crochet, M. Chhowalla, S. Tretiak, M. A. Alam, *Science* **2015**, *347*, 522.

[9] H. Zhou, Q. Chen, G. Li, S. Luo, T. B. Song, H. S. Duan, Z. Hong, J. You, Y. Liu, Y. Yang, *Science* **2014**, *345*, 542.

[10] W. Chen, Y. Wu, Y. Yue, J. Liu, W. Zhang, X. Yang, H. Chen, E. Bi, I. Ashraful, M. Grätzel, L. Han, *Science* **2015**, *350*, 944.

[11] V. D'Innocenzo, G. Grancini, M. J. Alcocer, A. R. Kandada, S. D. Stranks, M. M. Lee, G. Lanzani, H. J. Snaith, A. Petrozza, *Nat. Commun.* **2014**, *5*, 3586.

[12] N. Ahn, D. Y. Son, I. H. Jang, S. M. Kang, M. Choi, N. G. Park, *J. Am. Chem. Soc.* **2015**, *137*, 8696.

[13] NREL chart, www.nrel.gov/ncpv/images/efficiency_chart.jpg.

[14] B. Chen, Y. Bai, Z. Yu, T. Li, X. Zheng, Q. Dong, L. Shen, M. Boccard, A. Gruverman, Z. Holman, J. Huang, *Adv. Energy Mater.* **2016**. Available online. doi: 10.1002/aenm.201601128.

[15] J. P. Mailoa, C. D. Bailie, E. C. Johlin, E. T. Hoke, A. J. Akey, W. H. Nguyen, M. D. McGehee, T. Buonassisi, *Appl. Phy. Lett.* **2015**, *106*, 121105.

[16] S. Albrecht, M. Saliba, J. P. Correa Baena, F. Lang, L. Kegelmann, M. Mews, L. Steier, A. Abate, J. Rappich, L. Korte, R. Schlatmann, M. K. Nazeeruddin, A. Hagfeldt, M. Gratzel, B. Rech, *Energy Environ. Sci.* **2016**, *9*, 81.

[17] C. D. Bailie, M. G. Christoforo, J. P. Mailoa, A. R. Bowring, E. L. Unger, W. H. Nguyen, J. Burschka, N. Pellet, J. Z. Lee, M. Gratzel, R. Noufi, T. Buonassisi, A. Salleo, M. D. McGehee, *Energy Environ. Sci.* **2015**, *8*, 956.

[18] J. Werner, C. H. Weng, A. Walter, L. Fesquet, J. P. Seif, S. De Wolf, B. Niesen, C. Ballif, *J. Phys. Chem. Lett.* **2016**, *7*, 161.

[19] F. Fu, T. Feurer, T. Jager, E. Avancini, B. Bissig, S. Yoon, S. Buecheler, A. N. Tiwari, *Nat. Commun.* **2015**, *6*, 8932.

[20] J. Werner, G. Dubuis, A. Walter, P. Löper, S. J. Moon, S. Nicolay, M. M. Masis, S. De Wolf, B. Niesen, C. Ballif, *Sol. Energy Mater. Sol. Cells* **2015**, *141*, 407.

[21] D. P. McMeekin, G. Sadoughi, W. Rehman, G. E. Eperon, M. Saliba, M. T. Hörantner, A. Haghighirad, N. Sakai, L. Korte, B. Rech, M. B. Johnston, L. M. Herz, H. J. Snaith, *Science* **2016**, *351*, 151.

[22] J. Burschka, N. Pellet, S. J. Moon, R. H. Baker, P. Gao, M. K. Nazeeruddin, M. Gratzel, *Nature* **2013**, *499*, 316.

[23] W. Ke, C. Xiao, C. Wang, B. Saparov, H. S. Duan, D. Zhao, Z. Xiao, P. Schulz, S. P. Harvey, W. Liao, W. Meng, Y. Yu, A. J. Cimaroli, C. S. Jiang, K. Zhu, M. A. Jassim, G. Fang, D. B. Mitzi, Y. Yan, *Adv. Mater.* **2016**, *28*, 5214.

[24] P. W. Liang, C. Y. Liao, C. C. Chueh, F. Zuo, S. T. Williams, X. K. Xin, J. Lin, A. K. Jen, *Adv. Mater.* **2014**, *26*, 3748.

[25] C. G. Wu, C. H. Chiang, Z. L. Tseng, M. K. Nazeeruddin, A. Hagfeldt, M. Gratzel, *Energy Environ. Sci.* **2015**, *8*, 2725.

[26] X. Li, M. Ibrahim Dar, C. Yi, J. Luo, M. Tschumi, S. M. Zakeeruddin, M. K. Nazeeruddin, H. Han, M. Grätzel, *Nat. Chem.* **2015**, *7*, 703.

[27] M. Xiao, F. Huang, W. Huang, Y. Dkhissi, Y. Zhu, J. Etheridge, A. G. Weale, U. Bach, Y. B. Cheng, L. Spiccia, *Angew. Chem. Int. Ed.* **2014**, *53*, 9898.

[28] N. J. Jeon, J. H. Noh, Y. C. Kim, W. S. Yang, S. Ryu, S. I. Seok, *Nat. Mater.* **2014**, *13*, 897.

[29] M. Liu, M. B. Johnston, H. J. Snaith, *Nature* **2013**, *501*, 395.

[30] T. Zhang, M. Yang, Y. Zhao, K. Zhu, *Nano Lett.* **2015**, *15*, 3959.

[31] Q. Chen, H. Zhou, Z. Hong, S. Luo, H. S. Duan, H. H. Wang, Y. Liu, G. Li, Y. Yang, *J. Am. Chem. Soc.* **2014**, *136*, 622.

[32] Y. Wu, A. Islam, X. Yang, C. Qin, J. Liu, K. Zhang, W. Peng, L. Han, *Energy Environ. Sci.* **2014**, *7*, 2934.

[33] Q. Dong, Y. Yuan, Y. Shao, Y. Fang, Q. Wang, J. Huang, *Energy Environ. Sci.* **2015**, *8*, 2464.

[34] J. You, Y. Yang, Z. Hong, T. B. Song, L. Meng, Y. Liu, C. Jiang, H. Zhou, W. H. Chang, G. Li, Y. Yang, *Appl. Phys. Lett.* **2014**, *105*, 183902.

[35] K. Wang, C. Liu, P. Du, J. Zheng, X. Gong, *Energy Environ. Sci.* **2015**, *8*, 1245.

[36] C. H. Chiang, C. G. Wu, *Nat. Photonics* **2016**, *10*, 196.

[37] J. W. Lee, D. J. Seol, A. N. Cho, N. G. Park, *Adv. Mater.* **2014**, *26*, 4991.

[38] Z. K. Wang, M. Li, Y. G. Yang, Y. Hu, H. Ma, X. Y. Gao, L. S. Liao, *Adv. Mater.* **2016**, *28*, 6695.

[39] M. Saliba, T. Matsui, J.Y. Seo, K. Domanski, J. P. C. Baena, M. K. Nazeeruddin, S. M. Zakeeruddin, W. Tress, A. Abate, A. Hagfeldt, M. Gratzel, *Energy Environ. Sci.* **2016**, *9*, 1989.

[40] N. J. Jeon, J. H. Noh, W. S. Yang, Y. C. Kim, S. Ryu, J. Seo, S. I. Seok, *Nature* **2015**, *517*, 476.

[41] D. Bi, W. Tress, M. I. Dar, P. Gao, J. Luo, C. Renevier, K. Schenk, A. Abate, F. Giordano, J. P. C. Baena, J. D. Decoppet, S. M. Zakeeruddin, M. K. Nazeeruddin, M. Grätzel, A. Hagfeldt, *Sci. Advances* **2016**, *2*, e1501170.

[42] N. J. Jeon, J. Lee, J. H. Noh, M. K. Nazeeruddin, M. Gratzel, S. I. Seok, *J. Am. Chem. Soc.* **2013**, *135*, 19087.

[43] Z. Yu, L. Sun, *Adv. Energy Mater.* **2015**, *5*, 1500213.

[44] D. Liu, T. L. Kelly, *Nat. Photonics* **2014**, *8*, 133.

[45] F. Giordano, A. Abate, J. P. Correa Baena, M. Saliba, T. Matsui, S. H. Im, S. M. Zakeeruddin, M. K. Nazeeruddin, A. Hagfeldt, M. Graetzel, *Nat. Commun.* **2016**, *7*, 10379.

[46] P. Docampo, J. M. Ball, M. Darwich, G. E. Eperon, H. J. Snaith, *Nat. Commun.* **2013**, *4*, 2761.

[47] S. S. Shin, W. S. Yang, J. H. Noh, J. H. Suk, N. J. Jeon, J. H. Park, J. S. Kim, W. M. Seong, S. I. Seok, *Nat. Commun.* **2015**, *6*, 7410.

[48] J. T.W. Wang, J. M. Ball, E. M. Barea, A. Abate, J. A. A. Webber, J. Huang, M. Saliba, I. N. M. Sero, J. Bisquert, H. J. Snaith, *Nano lett.* **2013**, *14*, 724.

[49] C. Wang, D. Zhao, C. R. Grice, W. Liao, Y. Yu, A. Cimaroli, N. Shrestha, P. J. Roland, J. Chen, Z. Yu, P. Liu, N. Cheng, R. J. Ellingson, X. Zhao, Y. Yan, *J. Mater. Chem. A* **2016**. Available online. doi: 10.1039/C6TA04503K.

[50] S. Ryu, J. Seo, S. S. Shin, Y. C. Kim, N. J. Jeon, J. H. Noh, S. I. Seok, *J. Mater. Chem. A* **2015**, *3*, 3271.

[51] K. Wojciechowski, T. Leijtens, S. Siprova, C. Schlueter, M. T. Horantner, J. T. Wang, C. Z. Li, A. K. Jen, T. L. Lee, H. J. Snaith, *J. Phys. Chem. Lett.* **2015**, *6*, 2399.

[52] L. Zuo, Z. Gu, T. Ye, W. Fu, G. Wu, H. Li, H. Chen, *J. Am.Chem. Soc.* **2015**, *137*, 2674.

[53] H. Yoon, S. M. Kang, J. K. Lee, M. Choi, *Energy Environ. Sci.* **2016**, *9*, 2262.

[54] C. Tao, S. Neutzner, L. Colella, S. Marras, A. R. Srimath Kandada, M. Gandini, M. D. Bastiani, G. Pace, L. Manna, M. Caironi, C. Bertarelli, A. Petrozza, *Energy Environ. Sci.* **2015**, *8*, 2365.

[55] J. P. Correa Baena, L. Steier, W. Tress, M. Saliba, S. Neutzner, T. Matsui, F. Giordano, T. J. Jacobsson, A. R. Srimath Kandada, S. M. Zakeeruddin, A. Petrozza, A. Abate, M. K. Nazeeruddin, M. Gratzel, A. Hagfeldt, *Energy Environ. Sci.* **2015**, *8*, 2928.

[56] Q. Liu, M. C. Qin, W. J. Ke, X. L. Zheng, Z. Chen, P. L. Qin, L. B. Xiong, H. W. Lei, J. W. Wan, J. Wen, G. Yang, J. J. Ma, Z. Y. Zhang, G. J. Fang, *Adv. Funct. Mater.* **2016**. Available online. doi: 10.1002/adfm.201600910.

[57] Z. Yuan, Z. Wu, S. Bai, Z. Xia, W. Xu, T. Song, H. Wu, L. Xu, J. Si, Y. Jin, B. Sun, *Adv. Energy Mater.***2015**, *5*, n/a. Available online. doi: 10.1002/aenm.201500038.

[58] J. Y. Jeng, Y. F. Chiang, M. H. Lee, S. R. Peng, T. F. Guo, P. Chen, T. C. Wen, *Adv. Mater.* **2013**, *25*, 3727.

[59] K. Wojciechowski, M. Saliba, T. Leijtens, A. Abate, H. J. Snaith, *Energy Environ. Sci.* **2014**, *7*, 1142.

[60] P. Qin, A. L. Domanski, A. K. Chandiran, R. Berger, H. J. Butt, M. I. Dar, T. Moehl, N. Tetreault, P. Gao, S. Ahmad, M. K. Nazeeruddin, M. Gratzel, *Nanoscale* **2014**, *6*, 1508.

[61] S. K. Pathak, A. Abate, P. Ruckdeschel, B. Roose, K. C. Gödel, Y. Vaynzof, A. Santhala, S. I. Watanabe, D. J. Hollman, N. Noel, A. Sepe, U. Wiesner, R. Friend, H. J. Snaith, U. Steiner, *Adv. Funct. Mater.* **2014**, *24*, 6046.

[62] M. Lv, W. Lv, X. Fang, P. Sun, B. Lin, S. Zhang, X. Xu, J. Ding, N. Yuan, *RSC Adv.* **2016**, *6*, 35044.

[63] L. S. Oh, D. H. Kim, J. A. Lee, S. S. Shin, J. W. Lee, I. J. Park, M. J. Ko, N. G. Park, S. G. Pyo, K. S. Hong, J. Y. Kim, *J. Phys. Chem. C* **2014**, *118*, 22991.

[64] P. W. Liang, C. C. Chueh, S. T. Williams, A. K. Y. Jen, *Adv. Energy Mater.* **2015**, *5*, 1402321.

[65] B. M. Reddy, B. Chowdhury, P. G. Smirniotis, *Appl. Catal. A: Gen.* **2001**, *219*, 53.

[66] J. You, L. Meng, T. B. Song, T. F. Guo, Y. Yang, W. H. Chang, Z. Hong, H. Chen, H. Zhou, Q. Chen, Y. Liu, N. De Marco, Y. Yang, *Nat. Nanotechnology* **2016**, *11*, 75.

[67] C. O'Rourke, D. R. Bowler, *J. Phys. Chem. C* **2014**, *118*, 7261.

[68] T. Duong, N. Lal, D. Grant, D. Jacobs, P. Zheng, S. Rahman, H. Shen, M. Stocks, A. Blakers, K. Weber, T. P. White, K. R. Catchpole, *IEEE J. Photovoltaics* **2016**, *6*, 679.

[69] K. A. Bush, C. D. Bailie, Y. Chen, A. R. Bowring, W. Wang, W. Ma, T. Leijtens, F. Moghadam, M. D. McGehee, *Adv. Mater.* **2016**, *28*, 3937.

[70] E. Franklin, K. Fong, K. McIntosh, A. Fell, A. Blakers, T. Kho, D. Walter, D. Wang, N. Zin, M. Stocks, E.-C. Wang, N. Grant, Y. Wan, Y. Yang, X. Zhang, Z. Feng, P. J. Verlinden, *Prog. Photovoltaics: Res. Appl.* **2016**, *24*, 411.
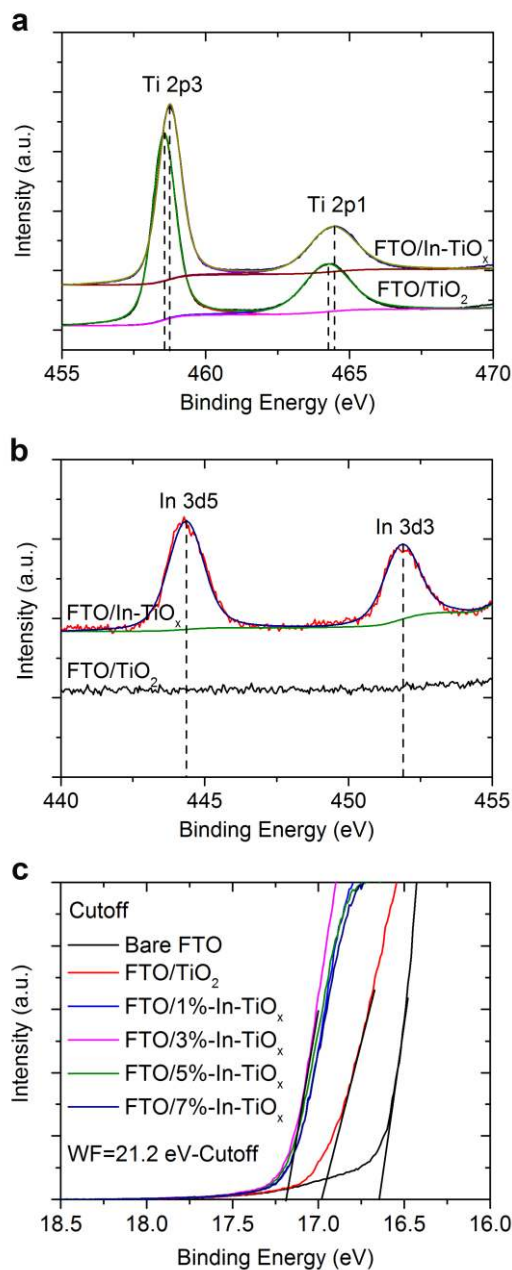
Figure 1. The XPS and UPS spectra of FTO/TiO$_2$ and FTO/In-TiO$_x$. a) XPS spectra of Ti 2p peaks; b) XPS spectra of In 3d peaks; c) UPS spectra of bare FTO, FTO/TiO$_2$ and FTO/In-TiO$_x$.
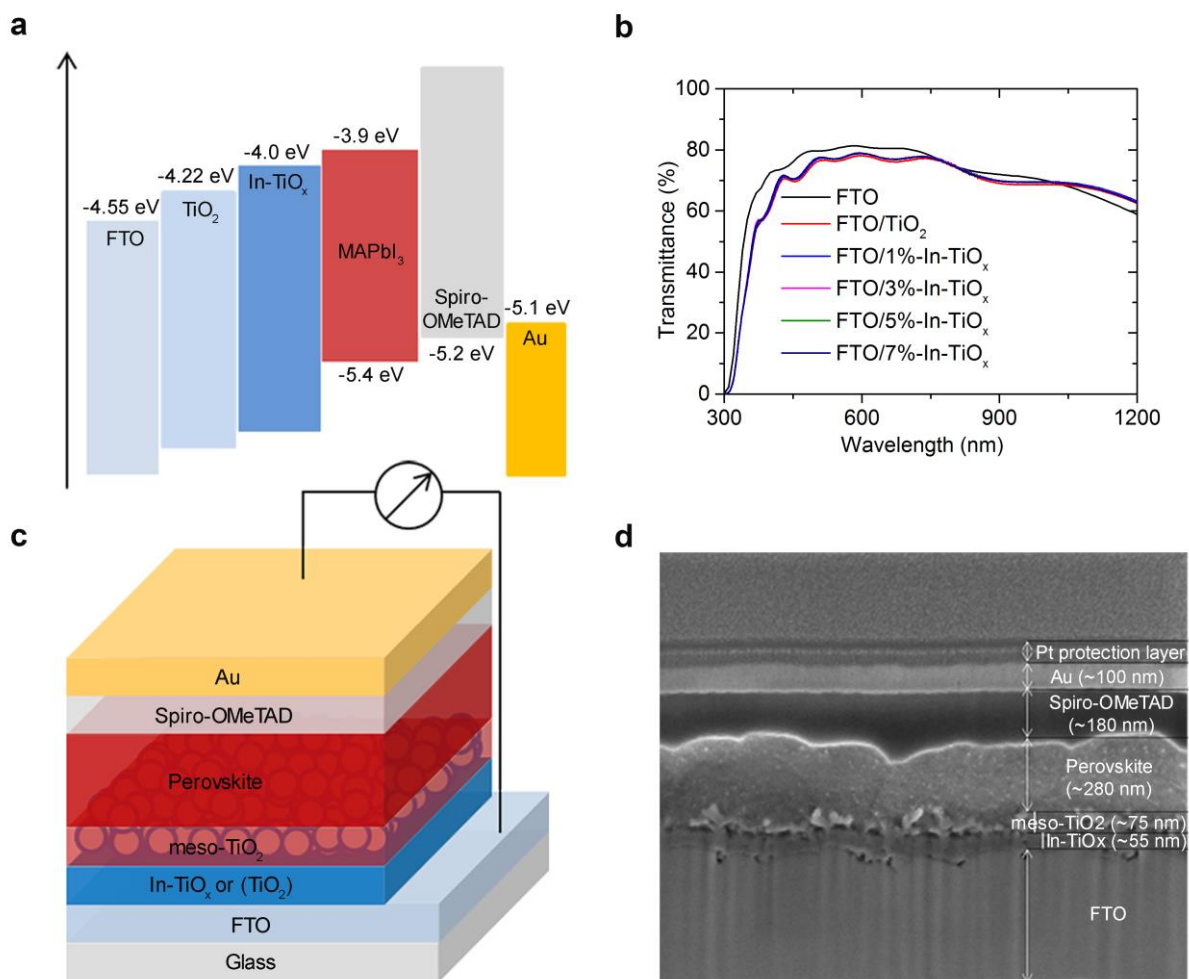
Figure 2. a) Diagram showing the energy levels of different materials. b) Transmittance spectra of bare FTO, FTO/TiO$_2$ and FTO/In-TiO$_x$. c) Schematic of the standard device structure studied here. d) SEM cross-sectional image of the device with a structure: FTO/In-TiO$_x$/meso-TiO$_2$/MAPbI$_3$/Spiro-OMeTAD/Au. Note that Pt protection layer was only used to prepare FIB SEM cross-sectional image.
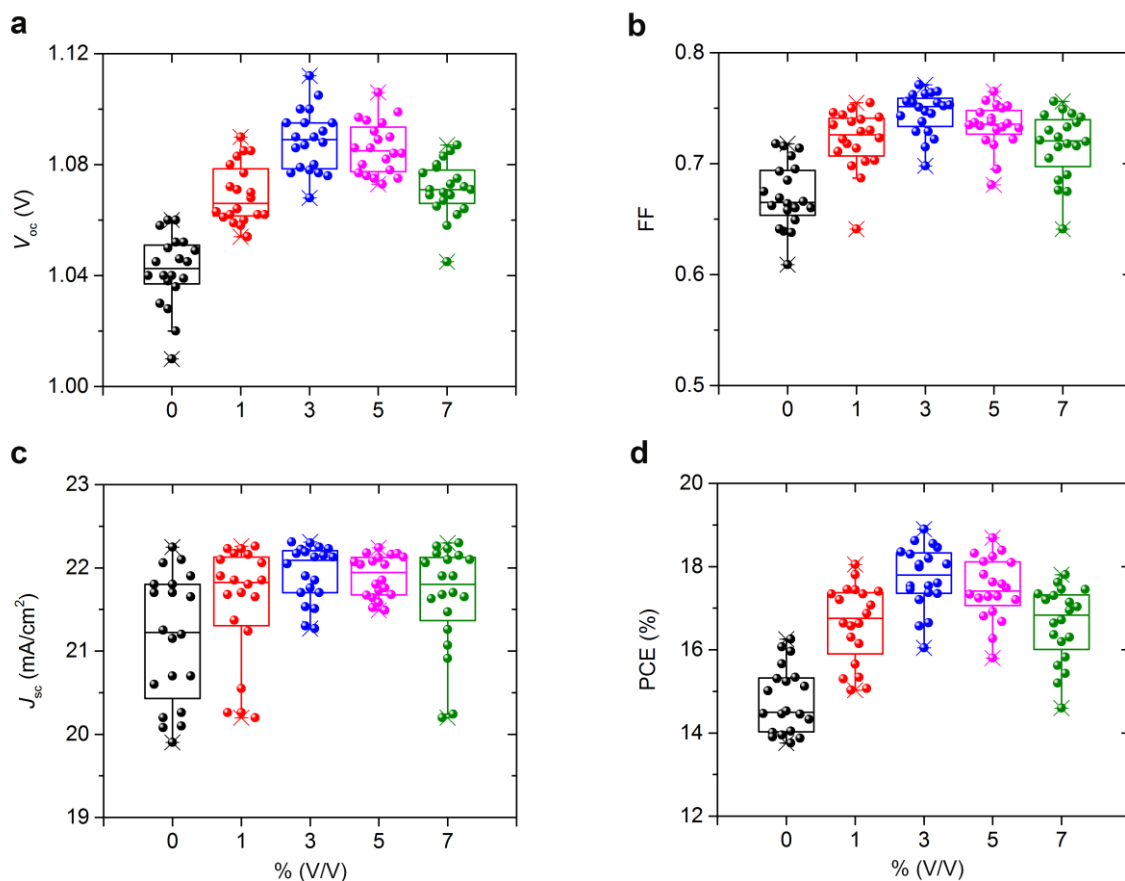
Figure 3. Statistical distribution of the photovoltaic parameters for cells with different indium doping concentrations, with a structure of FTO/In-TiO$_x$/meso-TiO$_2$/MAPbI$_3$/Spiro-OMeTAD/Au. a) Distribution of V_{oc}; b) distribution of FF; c) distribution of J_{sc}; d) distribution of PCE. Note that the 0% (v/v) condition is pure TiO$_2$. Results are shown for 100 cells (each condition has 20 cells) collected from 12 different batches. All devices were tested at a 50 mV/s reverse scan rate.
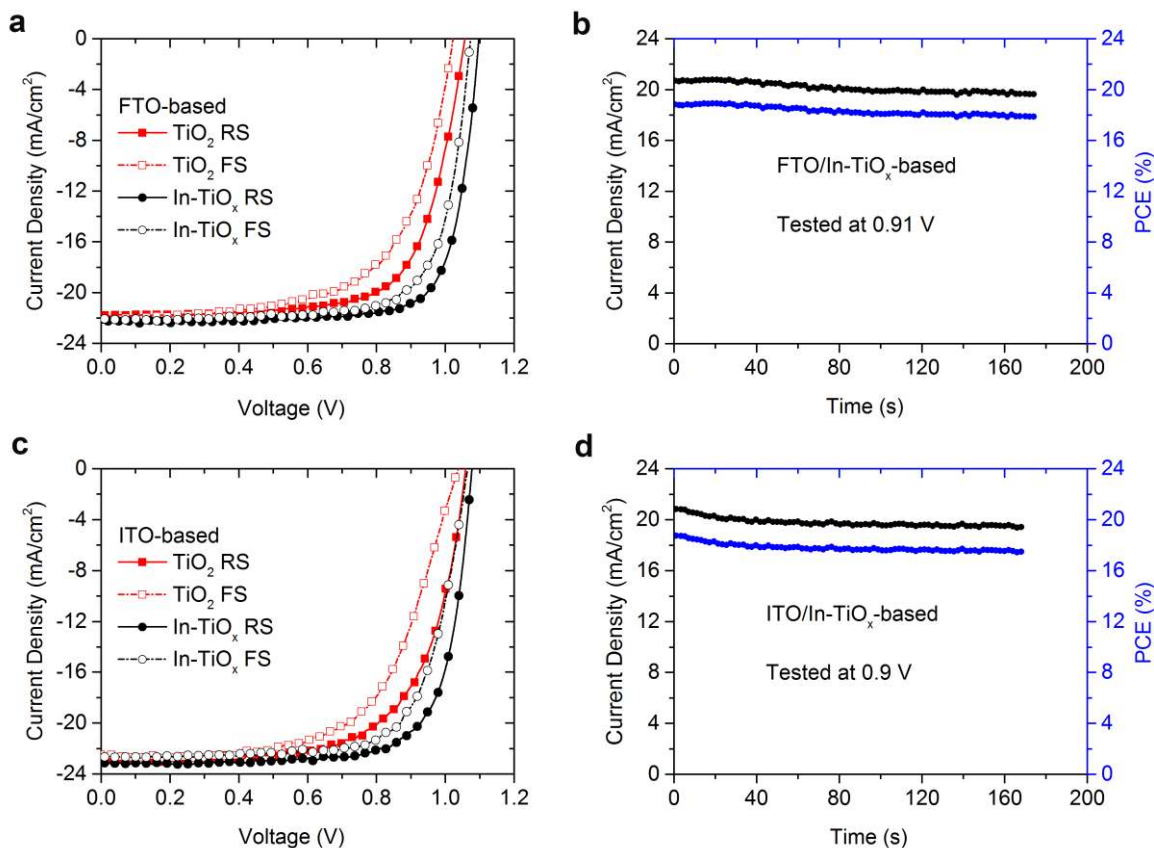
Figure 4. Photovoltaic performance of our champion devices. a) Current density-voltage curves of the FTO/In-TiO$_x$ (or TiO$_2$)/meso-TiO$_2$/MAPbI$_3$/Spiro-OMeTAD/Au cells; and b) steady-state current density and efficiency of the In-TiO$_x$-based cell tested at 0.91 V. c) Current density-voltage curves of the ITO/In-TiO$_x$ (or TiO$_2$)/meso-TiO$_2$/MAPbI$_3$/Spiro-OMeTAD/Au cells; and d) steady-state current density and efficiency of the In-TiO$_x$-based cell tested at 0.90 V. Note the legend label RS represents reverse scan (from V_{oc} to J_{sc}), and the FS represents forward scan (from J_{sc} to V_{oc}). All devices were tested at a 50 mV/s scan rate.
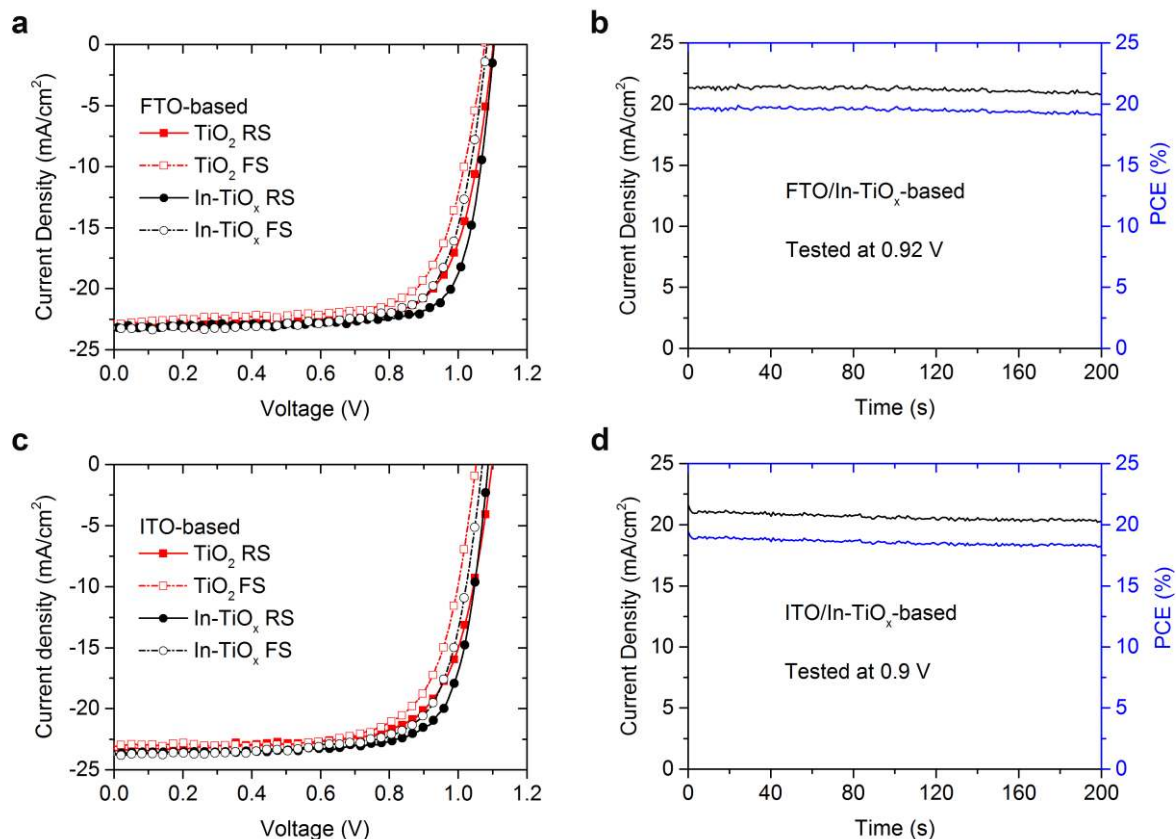
Figure 5. Photovoltaic performance of our champion Cs-mixed halide perovskite devices. a) Current density-voltage curves of the FTO/In-TiO$_x$ (or TiO$_2$)/meso-TiO$_2$/Cs-mixed halide perovskite/Spiro-OMeTAD/Au cells; and b) steady-state current density and efficiency of the In-TiO$_x$-based cell tested at 0.92 V. c) Current density-voltage curves of the ITO/In-TiO$_x$ (or TiO$_2$)/meso-TiO$_2$/Cs-mixed halide perovskite/Spiro-OMeTAD/Au cells; and d) steady-state current density and efficiency of the In-TiO$_x$-based cell tested at 0.90 V. Note that the Cs-mixed halide is Cs$_{0.05}$(MA$_{0.17}$FA$_{0.83}$)$_{0.95}$Pb(I$_{0.83}$Br$_{0.17}$)$_3$. The legend label RS represents reverse scan (from V_{oc} to J_{sc}), and FS represents forward scan (from J_{sc} to V_{oc}). All devices were tested at a 50 mV/s scan rate.
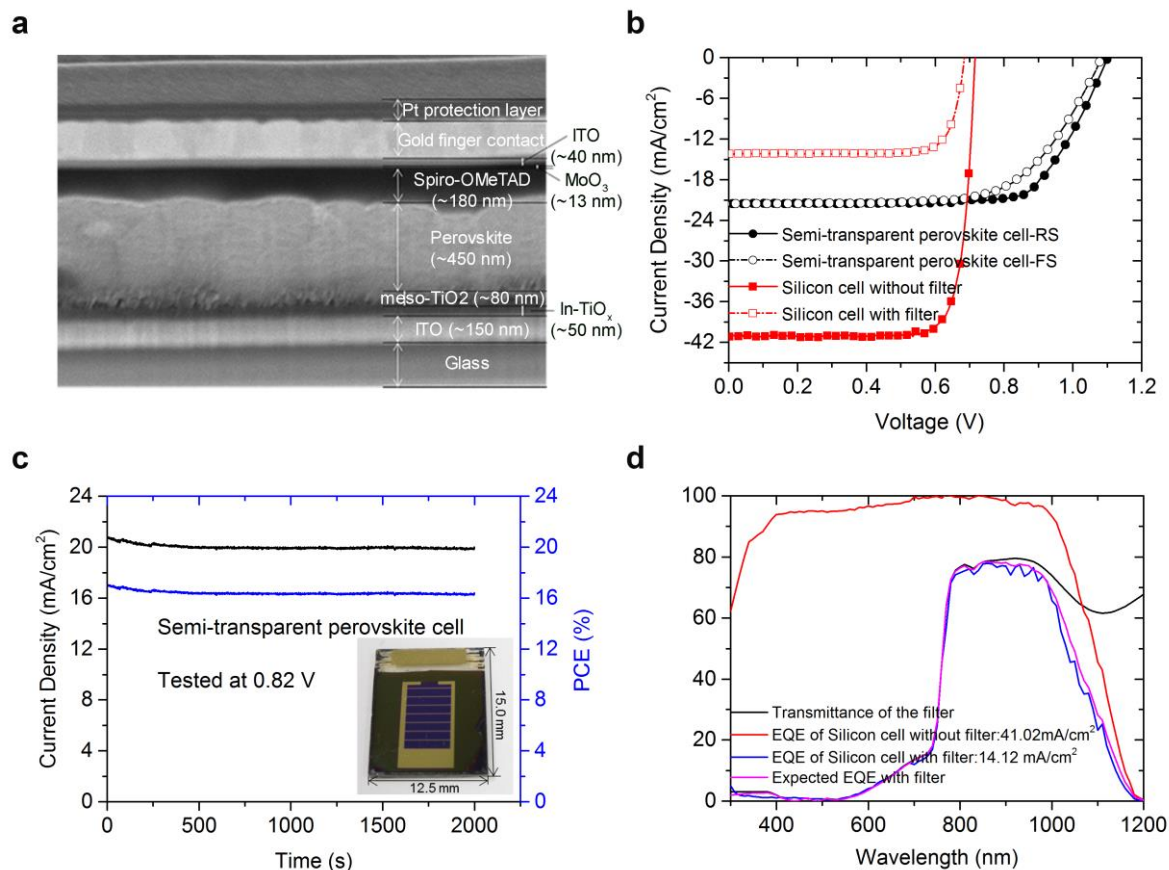
Figure 6. a) SEM cross-sectional image of the semi-transparent cell with a structure of ITO/In-TiO$_x$/meso-TiO$_2$/Cs-mixed halide perovskite/Spiro-OMeTAD/MoO$_3$/ITO/Gold finger contact. Note that Pt protection layer was only used to prepare FIB SEM cross-sectional image. b) Current density-voltage curves of the semi-transparent perovskite cell and IBC silicon cell. c) Steady-state current density and efficiency of the semi-transparent cell tested at 0.82 V. d) Transmittance of the semi-transparent cells and EQE of the IBC silicon cell with/without filter.

Table 1. Photovoltaic parameters of our champion devices with a structure of FTO/In-TiO$_x$ (or TiO$_2$)/meso-TiO$_2$/MAPbI$_3$/Spiro-OMeTAD/Au.

ETL	Scan direction	V_{oc} [V]	J_{sc} [mA/cm^2]	FF [%]	PCE [%]	R$_s$ [Ω cm^2]	R$_{sh}$ [Ω cm^2]	Steady-State Efficiency [%]
FTO/In-TiO$_x$	RS	1.10	22.3	77.1	18.9	4.1	1454	17.9
	FS	1.08	22.1	74.3	17.7	5.5	1309	
FTO/TiO$_2$	RS	1.06	21.8	70.6	16.3	6.8	1013	13.5
	FS	1.03	22.1	62.9	14.3	11.0	961	
ITO/In-TiO$_x$	RS	1.09	23.0	75.0	18.8	4.5	1241	17.5
	FS	1.07	22.6	72.2	17.4	6.3	1026	
ITO/TiO$_2$	RS	1.06	22.8	66.7	16.1	8.5	987	14.0
	FS	1.04	22.5	62.1	14.5	11.3	816	

Note that all devices were tested at a 50 mV/s scan rate under one sun (100 mW/cm^2, AM 1.5G); RS represents reverse scan (from V_{oc} to J_{sc}); FS represents forward scan (from J_{sc} to V_{oc}). R$_s$ represents series resistance and R$_{sh}$ represents shunt resistance.

Table 2. Photovoltaic parameters of our champion devices, with a structure: FTO/In-TiO$_x$ (or TiO$_2$)/mesoTiO$_2$/Cs$_{0.05}$(MA$_{0.17}$-FA$_{0.83}$)$_{0.95}$Pb(I$_{0.83}$Br$_{0.17}$)$_3$/Spiro-OMeTAD/Au.

ETL	Scan direction	V_{oc} [V]	J_{sc} [mA/cm^2]	FF [%]	PCE [%]	R$_s$ [Ω cm^2]	R$_{sh}$ [Ω cm^2]	Steady-State Efficiency [%]
FTO/In-TiO$_x$	RS	1.10	23.1	79.1	20.1	3.4	1647	19.3
	FS	1.09	23.2	74.0	18.7	5.2	1351	
FTO/TiO$_2$	RS	1.10	22.9	74.5	18.8	4.7	1264	18.1
	FS	1.08	23.1	70.7	17.6	7.1	1104	
ITO/In-TiO$_x$	RS	1.09	23.6	76.2	19.6	4.0	1326	18.4
	FS	1.07	23.7	73.1	18.5	5.7	1301	
ITO/TiO$_2$	RS	1.10	23.4	71.1	18.3	6.5	1124	17.4
	FS	1.06	23.1	70.2	17.2	6.8	1012	

Table 3. Photovoltaic parameters of the four-terminal tandem cells.

|		V_{oc} [V]	J_{sc} [mA/cm^2]	FF [%]	PCE [%]	Steady-State Efficiency (%)
Perovskite (top cell)	RS	1.10	21.5	73.5	17.4	16.6 (after 200 s)
	FS	1.09	21.5	65.4	15.3	
IBC silicon (bottom cell)	Without filter	0.72	41.0	81.3	24.0	24.0
	With filter	0.69	14.2	81.0	7.9	7.9
Four-terminal tandem cell						24.5

Solution-processed, indium-doped TiOx films are shown to be very effective electron transport/hole-blocking layers for high-performance perovskite cells. Doping improves the conductivity and work-function energy alignment at the ETL/perovskite interface, leading to high fill-factor and open-circuit voltage. An efficiency of ~19.3% is demonstrated for a perovskite cell, and a steady-state efficiency of 24.5% is presented for a four-terminal perovskite-silicon tandem cell.

Jun Peng,* The Duong, Xianzhong Zhou, Heping Shen, Yiliang Wu, Hemant Kumar Mulmudi, Yimao Wan, Dingyong Zhong, Juntao Li, Takuya Tsuzuki, Klaus J. Weber, Kylie R. Catchpole, and Thomas P. White*

Title: Efficient Indium-Doped TiO$_X$ Electron Transport Layers for High-Performance Perovskite Solar Cells and Perovskite-Silicon Tandems
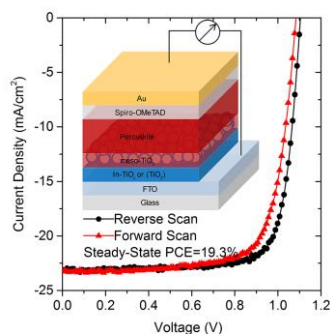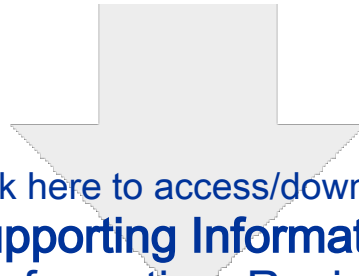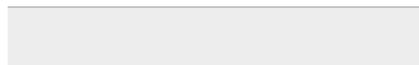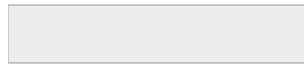
Click here to access/download
Supporting Information
Supporting Information_Revised_Final.doc

Click here to access/download
Production Data
2528_checklist.pdf